Chemical Science

EDGE ARTICLE

View Article Online
View Journal | View Issue

Cite this: *Chem. Sci.*, 2019, **10**, 10170

All publication charges for this article have been paid for by the Royal Society of Chemistry

Unusual near infrared (NIR) fluorescent palladium(II) macrocyclic complexes containing M–C bonds with bioimaging capability†

Yuhang Yao,[a] Chun-Liang Hou,[b] Zi-Shu Yang,[a] Guangliu Ran,[c] Lei Kang,[d] Cuicui Li,[d] Wenkai Zhang, *[c] Jing Zhang*[b] and Jun-Long Zhang *[a]

Near infrared (NIR) luminescent metal complexes are promising probes in bioimaging and biosensing, however they generally suffer from oxygen interference arising from heavy metal effects. We designed new tetradentate macrocyclic benzitripyrrin (C^N^N^N) ligands by combination of M–C bond formation and reducing the π-conjugation to achieve NIR fluorescent Pd complexes (700–1000 nm) with quantum yields up to 14%. To understand the origin of NIR fluorescence, detailed analyses by density functional theory/time-dependent density functional theory (DFT/TDDFT) calculations together with femtosecond and nanosecond transient absorption spectroscopies suggest that M–C bond formation indeed leads to destabilization of the d–d excited state and less effective quenching of emission; and importantly, small spin–orbital coupling (SOC) and the large singlet-triplet energy gap are the primary causes of the non-population of triplet states. Comparison of Pd^{II} and Pt^{II} analogues shows that the non-radiative channel of the out-plane vibration of the tripyrrin plane effectively quenches the fluorescence of the Pt^{II} complex but not the Pd^{II} congener. We also demonstrate the proof-of-concept applications of Pd^{II} complexes (**Pd-1** and **Pd-3**) encapsulated in silica nanoparticles, in both *in vitro* and *in vivo* bioimaging experiments without oxygen interference. Moreover, pH-induced reversible switching of NIR fluorescence was achieved even intracellularly using the Pd complex (**Pd-2**), which shows the potential to further develop perspective stimuli-responsive NIR materials.

Received 13th August 2019
Accepted 11th September 2019

DOI: 10.1039/c9sc04044g

rsc.li/chemical-science

Introduction

Imaging in the near infrared (NIR) region (700–1700 nm), known as the biological transparency window, attracts increasing attention for its unique advantages such as low tissue auto-absorption, small photon scattering, and deep tissue penetration, which is highly desirable to improve disease detection and treatment in clinical applications.[1] Exploring NIR molecular fluorophores with both high luminescence efficiency and biocompatibility, to circumvent the safety issues such as toxicity and metabolism arising from inorganic and carbon-based nanomaterials such as carbon nanotubes, quantum dots, and Ln doped nanoparticles, is essential to boost clinical translations.[2] Toward this goal, many organic fluorophores such as cyanines, donor–acceptor–donor (D–A–D) dyes, and borondipyrromethanes have been extensively studied as promising candidates in NIR imaging.[3] In sharp contrast to the tremendous progress made by organic fluorophores, metal coordination compounds that are equally important molecular fluorophores have been seldom employed as the candidates in NIR biological imaging.[4] Metal complexes possess intriguing photophysical properties such as brightness, large Stokes shifts, long lifetimes and anti-photobleaching and have been extensively used in visible bioimaging.[5] However, they generally suffer from severe photocytotoxicity because the population of triplet states arising from heavy metal effects initiates reactive oxygen species such as $^1O_2$, $O_2^{\bullet-}$ *etc.*, which hamper the direct application in NIR bioimaging. As such, further effort is required to design NIR metal complexes on par with their organic counterparts in biological applications.

Thanks to the fast growth of palladacycles,[6] notable examples of luminescent Pd^{II} complexes containing Pd–C bonds have emerged, because introducing a strong σ-donating carbanion

[a]*Beijing National Laboratory for Molecular Sciences, State Key Laboratory of Rare Earth Materials Chemistry and Applications, College of Chemistry and Molecular Engineering, Peking University, Beijing 100871, P. R. China. E-mail: zhangjunlong@pku.edu.cn*

[b]*Center of Materials Science and Optoelectronics Engineering, College of Materials Science and Opto-Electronic Technology, University of Chinese Academy of Sciences, Beijing 100049, P. R. China. E-mail: zhangj271@ucas.ac.cn*

[c]*Center for Advanced Quantum Studies, Department of Physics and Applied Optics Beijing Area Major Laboratory, Beijing Normal University, Beijing 100875, P. R. China. E-mail: wkzhang@bnu.edu.cn*

[d]*Department of Nuclear Medicine, Peking University First Hospital, Beijing 100034, P. R. China*

† Electronic supplementary information (ESI) available. CCDC 1912139–1912141. For ESI and crystallographic data in CIF or other electronic format see DOI: 10.1039/c9sc04044g

can destabilize the antibonding $4d_{x^2-y^2}$ orbital, allow metal to ligand charge transfer and thus enhance the luminescence.[6,7] However, extending this strategy to Pd^{II} porphyrinoids, which are typical phosphorescent complexes as red/NIR photosensitizers or probes (Fig. 1a),[6,7] to improve NIR luminescence has not been successful. Replacement of one of the pyrrolic nitrogen donors by a σ-donating carbanion afforded carbaporphyrinoids including N-confused porphyrins (Fig. 1b)[8] previously developed by Lash, Latos-Grazynski, Furuta and others. Deprotonation of the inner C–H bonds indeed offers the opportunity to form Pd–C bonds in porphyrin macrocycles, yet their photophysical properties have been much less frequently reported.[8] Another issue is the extent of π-conjugation. Che *et al.* pointed out the importance of the π-conjugation of ligands on the excited states and photophysical properties, for example, increasing π-conjugation leads to more allowed low-lying singlet transitions for the lowest triplet state to borrow intensity from and more likely displays phosphorescence than fluorescence.[9] By taking advantage of the merits of each approach, we reason that incorporation of O-bridging to replace the methine linker reduces the extent of the π-conjugation (Fig. 1c), which might give rise to new ligands with electronic structures different from those of traditional N_4 or CN_3 porphyrinoids.[10] Importantly, we envision that this design could impact upon the photophysical properties and achieve NIR fluorescent Pd^{II} complexes to minimize the oxygen interference.

In this work, we synthesized a series of new macrocyclic tetradentate C^N^N^N ligands, namely benzitripyrrin, (1^1E,1^2Z,5^1E,5^2Z)-2,4-bis(perfluorophenyl)-1^2H,3^1H,5^2H-6,8-dioxa-1,3,5(2,5)-tripyrrola-7(1,3)-benzenacyclo-octaphane derivatives, (**1–5**) by connecting tripyrrin with 1,3-dihydroxybenzene (resorcinol) derivatives (Fig. 1c). Surprisingly, Pd^{II} complexes displayed strong NIR fluorescence (700–1000 nm) with quantum yields up to 14%, but not the phosphorescence often observed in Pd^{II} porphyrins,[11] while the Pt(II) congener displays negligible NIR fluorescence. To the best of our knowledge, only a handful of Pd fluorescent complexes in the visible to deep red region have been previously reported.[12] Rybtchinski *et al.* ascribed the lack of phosphorescence to the weak electronic interactions between the metal centers and ligand π-system.[13] To gain insight into the luminescence mechanism, we performed fs/ns transient absorption (TA) spectroscopy and density functional theory/time-dependent density functional theory (DFT/TDDFT) calculations so that comparisons between Pd^{II} and Pt^{II} systems can be made. In view of the strong NIR fluorescence of the Pd complexes, proof-of-concept applications are performed in living cell imaging as well as *in vivo* imaging using a mice model by encapsulating Pd^{II} complexes including a pH sensitive compound into the nanochannels of mesoporous silica nanoparticles (MSN). Collectively, this work offers a new molecular scaffold to design NIR fluorescent Pd^{II} complexes with the capability of bioimaging without oxygen interference.

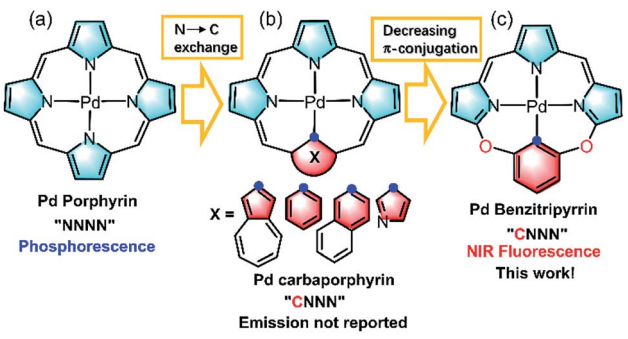

Fig. 1 Schematic view of the ligand design: (a) porphyrinoids, (b) carbaporphyrinoids, and (c) benzitripyrrins.

Results and discussion

Synthesis and characterization

As shown in Scheme 1a, we synthesized a series of new tripyrrin ligands (1^1E,1^2Z,5^1E,5^2Z)-2,4-bis(perfluorophenyl)-1^2H,3^1H,5^2H-6,8-dioxa-1,3,5(2,5)-tripyrrola-7(1,3)-benzenacyclooctaphane with different substituents on the bridging phenyl group (**1–5**, $R_1 = R_2 = H$, **1**; $R_1 = NMe_2$, $R_2 = H$, **2**; $R_1 = CN$, $R_2 = H$, **3**; $R_1 = H$, $R_2 = OMe$, **4**; $R_1 = H$, and $R_2 = CN$, **5**) in 3 steps.[10] Synthesis of the Pd^{II} (**Pd-1–3**) or Pt^{II} (**Pt-1**) complexes was achieved in the yields of *ca.* 10–25%. **1–5**, **Pd-1–3** and **Pt-1** have been characterized using HR ESI-MS, ^1H, ^{13}C and ^{19}F NMR, FT-IR spectrometers and spectroscopes and the detailed synthetic procedures are listed in the ESI (Schemes S1–S11, Fig. S1–S45†).

Single crystals of **1**, **Pd-1** and **Pt-1** suitable for X-ray diffraction were obtained by slow diffusion of hexane to chloroform solution (CCDC: 1912139, 1912140, 1912141 in Table S1†). As shown in Scheme 1b and Fig. S46–S48,†**1** displays a larger N_3C cavity than carbaporphyrin with a distance of opposite N atoms of ~3.96 Å. **Pd-1** and **Pt-1** show a planar-square structure with the average Pd–N/Pt–N bond distances of ~2.01 Å. The short distances of 2.00 and 2.01 Å of the M–C bond are shown in **Pd-1**

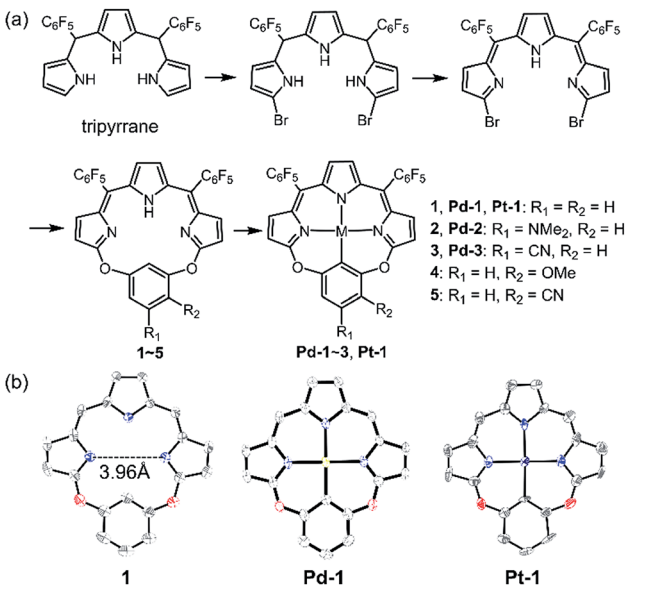

Scheme 1 (a) Synthetic routes of **1–5**, **Pd-1–3** and **Pt-1**. (b) X-ray crystal structures of **1**, **Pd-1** and **Pt-1**. Hydrogen atoms, meso-substituents and solvent molecules are omitted for clarity.

and **Pt-1**, respectively, which are comparable to those (1.95–2.06 and 1.95–2.05 Å) observed in palladacycles or platinum complexes.[7]

Photophysical properties

Absorption and emission spectra of **1–5**, **Pd-1–3** and **Pt-1** were recorded at 298 K in CH_2Cl_2 (Fig. 2 and S49–S77†) and the photophysical data are tabulated in Table S2.†**1–5** show a sharp and intense band at around 300–400 nm and a broad, split band at 500–600 nm with extinction coefficients in the order of 10^4 $dm^3\ mol^{-1}\ cm^{-1}$. The absorption could be assigned to the intraligand (IL) [$\pi \rightarrow \pi^*$] transitions.[10] Interestingly, the aryl substitution has a slight effect on the absorption of **1–5**, indicating that the vertical transition mainly involves HOMO → LUMO transition localized on the tripyrrin core.[10] Upon excitation at 500 nm, **1**, **3** and **5** display intense vibronic-structured emission with a maximum at 600 or 615 nm, while **2** and **4** show a weak, structureless emission around 550–800 nm. It is worthy to note that the electron-donating NMe_2 quenches the fluorescence of **2**, probably due to the photoinduced electron transfer (PET) process.[14]

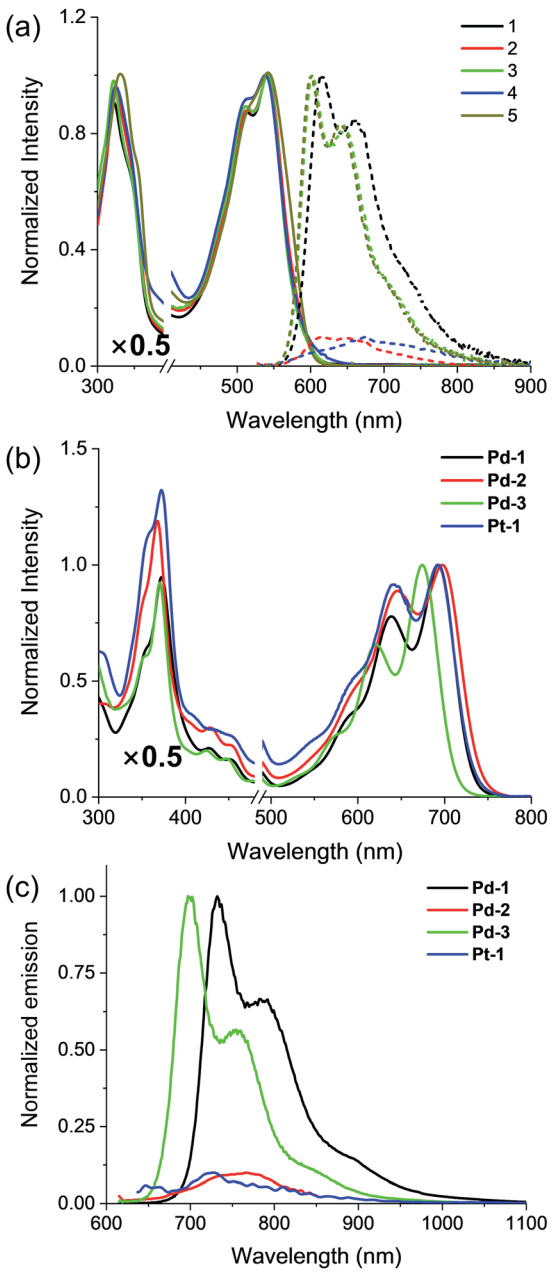

Fig. 2 (a) Absorption (solid line) and emission (dashed line) spectra of the free base ligands **1–5** and (b) absorption and (c) emission spectra of **Pd-1–3** and **Pt-1** in CH_2Cl_2.

Pd-1–3 and **Pt-1** exhibit a sharp and intense absorbance in the range of 320–400 and 500–750 nm, with red-shifts of *ca.* 45 nm in the high energy region (320–400 nm) and *ca.* 150 nm in the low energy region (500–750 nm) compared to the corresponding ligands. With the electron-withdrawing CN, **Pd-3** leads to a *ca.* 17 nm hypsochromic shift to **Pd-1**, while **Pd-2** displays a bathochromic shift of *ca.* 8 nm. This indicates the more significant effect of the aryl substituents on the metal complexes than on the ligands. Upon excitation at 600 or 700 nm, all of the metal complexes emit at 700–1000 nm, red-shifts of *ca.* ~130 nm compared to the corresponding ligands (Fig. 2c). Interestingly, exposure of such a solution to air does not quench the emission (Fig. S49–S52†). The emission lifetimes are in the nanosecond scale (<4 ns) even in 77 K glass (Fig. S65–S67†). Small Stokes shifts (<40 nm) are observed under either aerobic or anaerobic conditions. These photophysical data are suggestive of fluorescence for **Pd-1–3** and **Pt-1**. Among them, **Pd-1** and **Pd-3** exhibit intense fluorescence maxima at 732 and 700 nm with a vibronic band at 792 and 758 nm ($\Phi_F = 6.0$ and 14.0%, τ = 1.06 and 2.40 ns), respectively, while **Pd-2** displays a weak, less discernible vibrational emission centered at 767 nm with bi-exponential decay lifetimes of 0.26 (9%) and 2.05 ns (91%). **Pt-1** also exhibits a weak fluorescence centered at 729 nm with a bi-exponential decay lifetime of 0.17 (20%) and 3.34 ns (80%). As shown in Fig. S77,† decreasing temperature from 300 to 77 K enhances the emission of **Pt-1** (~5.2 fold) more than that of **Pd-1** (~1.3 fold), indicating that emission of **Pt-1** is more temperature- and vibration-dependent and will be discussed in context.

Electrochemical properties

The redox properties of **1**, **Pd-1** and **Pt-1** were examined by cyclic voltammetry (CV) using tetra-*n*-butylammonium hexafluorophosphate ($^nBu_4NPF_6$, 0.1 M) as the supporting electrolyte (Fig. 3, S78–S80†) and Table S3† summarizes the electrochemical data. Two quasi-reversible reduction waves at about −0.85 and −1.03 V *vs.* SCE and one irreversible oxidation wave at *ca.* 1.25 V *vs.* SCE are tentatively assigned to the cyclic tripyrrin ligand-centered redox potentials for **1** (Fig. S78†), similar to the previously reported cyclic tripyrrins (E_{red} = −0.92, −1.17 V and E_{ox} = 1.35 V).[10] **Pd-1** and **Pt-1** display two quasi-reversible reduction waves (−0.75 and −1.18 V *vs.* SCE for **Pd-1**, −0.67 and −1.11 V *vs.* SCE for **Pt-1**, Fig. 3a) and one irreversible oxidation wave (1.45 V *vs.* SCE for **Pd-1**, 1.25 V *vs.* SCE for **Pt-1**, Fig. 3a). These results suggest that both reduction and

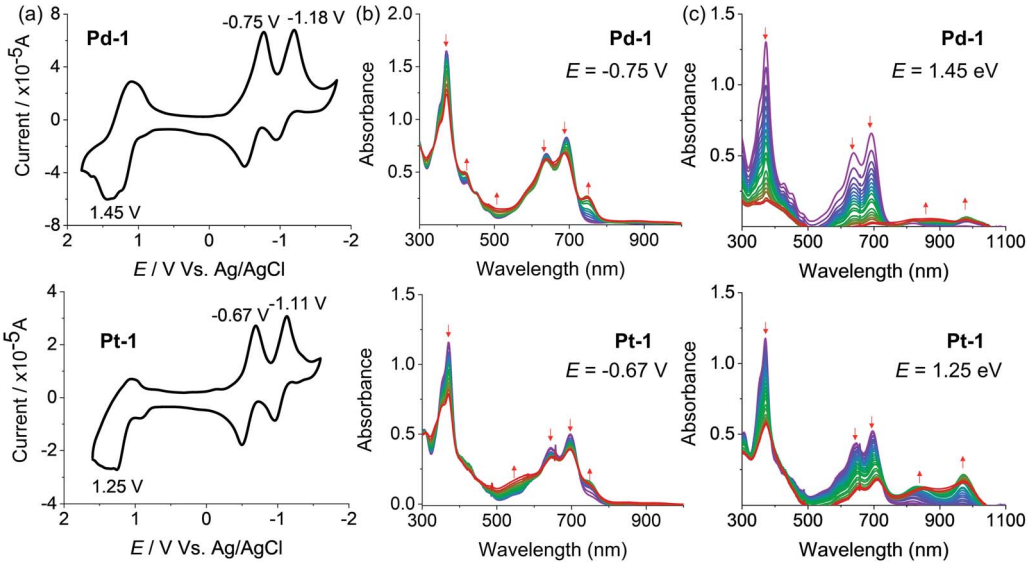

Fig. 3 (a) Cyclic voltammograms and spectroelectrochemistry at (b) reduction potentials (−0.75 and −0.67 V, respectively) and (c) oxidation potentials (1.45 and 1.25 V, respectively) of **Pd-1** and **Pt-1** in CH_2Cl_2.

oxidation are cyclic tripyrrin ligand-centered with mixing of the metal-centered contribution.

The spectroelectrochemistry of **1**, **Pd-1** and **Pt-1** were performed to monitor the spectral changes during the reduction and oxidation processes. As shown in Fig. S79,† one-electron reduction of **1** at −0.85 V causes a decreased absorption centered at 320 and 500 nm, and new peaks centered at 420, 600 and 750 nm appear with an isosbestic point at 366, 471 and 540 nm. One-electron reduction of **Pd-1** at −0.75 V and **Pt-1** at −0.67 V causes a slightly decreased absorption at 373, 640 and 692 nm with the appearance of a new peak at ∼750 nm (Fig. 3b). Such bands could be ascribed to the feature of the anionic radicals of the ligands. Oxidation of **1** at 1.25 V slightly decreases the absorption at 323, 508 and 540 nm, and new absorption centered at 380 and 600 nm appears with an isosbestic point at 350, 453 and 556 nm (Fig. S80†). When **Pd-1** or **Pt-1** was oxidized at *ca.* 1.45 or 1.25 V, respectively, the absorption intensity sharply decreases with a slight red-shift, and a new broad absorption peak at 750–1050 nm appears assigned to the cationic radicals (Fig. 3c).

Transient absorption spectroscopy

Insights into the nature of the excited states, exemplified by **Pd-1** and **Pt-1**, were obtained using nanosecond (ns) and femtosecond (fs) transient absorption (TA) spectroscopes in degassed tetrahydrofuran (THF). The ns-TA spectra display negligible signals of ground-state bleaching (GSB) (Fig. S81–S83†) upon excitation at 355 nm, indicating that there is no population of the triplet excited state for **Pd-1** and **Pt-1**. This is consistent with no phosphorescence observed in degassed solution or glass state in 77 K.

Fig. 4 shows the contour plot of the time-resolved absorption difference spectra for **Pd-1** and **Pt-1** upon excitation at 700 nm. We observed a GSB band maximum at 700 nm and the excited-state absorption (ESA) band centered in the range of 750–850 nm and 875–925 nm for **Pd-1**. **Pd-1** displays single exponential decay lifetime of 1.28 ns at 770 nm and bi-exponential decay lifetimes (86.34 ps and 1.32 ns) as monitored at 910 nm (Fig. 4c). This is assigned to the structural relaxation dynamics (∼100 ps) and intrinsic S_1 state lifetime (Table S2†). The ESA bands at 910 nm for **Pd-1** and ∼950 nm for **Pt-1** are identical to the absorption under one electron oxidation (Fig. 3c), suggesting that the structures at the singlet state may be similar to the cation radicals of **Pd-1** and **Pt-1**.

More importantly, in the range of 10–100 ps, **Pt-1** shows a new band around 758 nm accompanied with a simultaneous vanishing of ESA at 796 nm and a clear isosbestic point at 770 nm (Fig. 4d). As shown in Fig. 4d, a fast decay with tri-exponential lifetimes (0.20, 4.67 and 16.34 ps) at 796 nm decreases accompanied with a simultaneous appearance (0.046, 0.78 and 8.75 ps) of a new peak at 758 nm, followed by a single exponential decay lifetime of 3.77 ns comparable to the fluorescence lifetime of **Pt-1** (Table S2†). This suggest a fast energy transfer (within 100 ps) from the intrinsic S_1 state of **Pt-1** to a dark state, which might quench emission. We assumed this to be a vibrational state, usually in accordance with the time range of the structural relaxation (10–100 ps). Thus the S_1 excited state of **Pt-1** is probably deactivated by this non-radiative vibrational state, which is ascribed to a more temperature- and vibration-dependent fluorescence (Fig. S77†).

Computational studies

Pd^{II} and Pt^{II} complexes are well-known phosphorescent emitters due to the heavy-metal effect with large spin–orbit coupling (SOC) constants (ζ_{SOC} = 1504 and 4481 cm^{-1} for Pd^{II} and Pt^{II}).[15] However, increasing examples demonstrated that incorporation of a heavy metal does not guarantee efficient ISC and the structure and the nature of ligands also play important roles.[16]

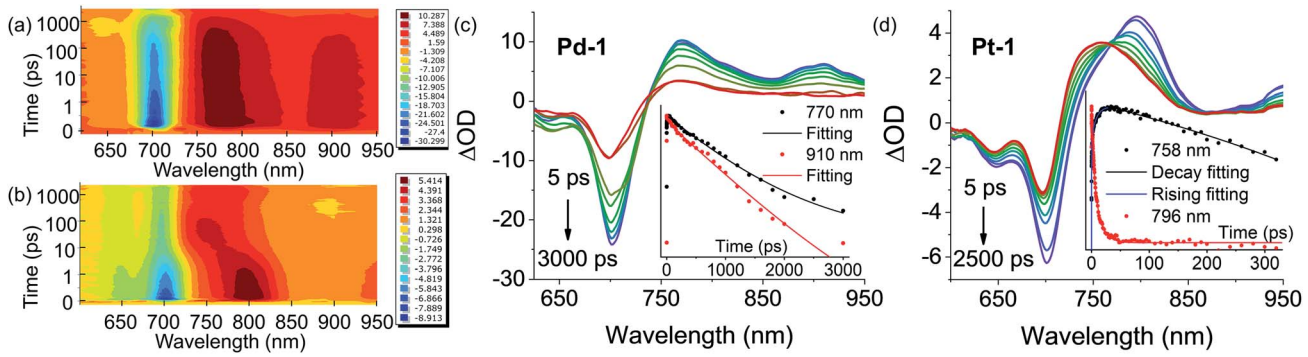

Fig. 4 Contour plot of time-resolved absorption difference spectra of (a) **Pd-1** and (b) **Pt-1** for time delays up to 3000 ps in the range of 600–950 nm in toluene. Femtosecond transient absorption (fs-TA) difference spectra of (c) **Pd-1** and (d) **Pt-1** recorded at selected decay times in toluene at 298 K. Insert: ESA kinetic decay traces at the specified wavelengths and lifetimes: fitting with exponential decay for (c) **Pd-1** ($\tau = 1281$ ps, $R^2 = 0.996$ at 770 nm; $\tau_1 = 86.34$ ps, $\tau_2 = 1318$ ps, and $R^2 = 0.996$ at 910 nm) and (d) **Pt-1** ($\tau = 3773$ ps and $R^2 = 0.982$ at 758 nm for curve decay at 758 nm; $\tau_1 = 0.046$ ps, $\tau_2 = 0.78$ ps, $\tau_3 = 8.75$ ps, and $R^2 = 0.995$ for curve rising at 758 nm; $\tau_1 = 0.20$ ps, $\tau_2 = 4.67$ ps, $\tau_3 = 16.34$ ps, and $R^2 = 0.988$ at 796 nm).

To understand the unusual fluorescence of Pd^{II} and Pt^{II} complexes, we investigated the electronic structures of **1–5**, **Pd-1** and **Pt-1** using DFT and TDDFT calculations. Electron-donating substituents (NMe_2 and OMe) destabilize both HOMO and LUMO in **2** and **4**, while the electron-withdrawing substituent (cyano group) stabilizes them in **3** and **5** (Fig. S84†). TDDFT results indicate that the vertical π–π* excitations are localized in tripyrrin moiety (Fig. S84 and Table S4†) for **1** and **3–5**. In **2**, the charge transfers from the bridging phenyl group to the tripyrrin moiety, similar to photoinduced electron transfer (PET).[14] Metal coordination stabilizes the LUMO and destabilizes the HOMO and thus narrows the HOMO–LUMO gap (Fig. S85†), which induces a red-shifted absorption. All the FMOs in **Pd-1** and **Pt-1** are ligand-centered.[18] The natural localized molecular orbital (NLMO) analysis[18b,19] reveals that the C-donor atom of the M–C bond shows sp^3-like behavior, different from sp^2-carbons in the benzene ring (Fig. S86†), which is suggestive of the σ-donating nature, analogous to the M–C bond in previously reported complexes of benziporphyrin and carbaporphyrin.[8c,8e] Formation of M–C bonds largely stabilizes the metal-centered bonding orbitals (Fig. S87†). The splitting (Δdd*) between the occupied and unoccupied d orbitals is found to be quite large for **Pd-1** (5.78 eV) and **Pt-1** (6.70 eV). This indicates that the non-radiative decay channels through the MC dd excited states could be excluded for **Pd-1** and **Pt-1**.

For **Pd-1** and **Pt-1**, their S_1 states are 6640 and 7292 cm^{-1} above the T_1 state, 2135 and 59 cm^{-1} below the T_2 state (Tables S5 and S6†). The calculated ISC rate constants using the MOMAP program[20] are given in Fig. 5a and Table S7,† as well as the radiative and non-radiative rate constants of S_1 states. Since the ΔE_{ST} are large (0.82 and 0.60 eV for **Pd-1** and **Pt-1**), the spin–orbit coupling values are estimated to be 0.82 and 0.60 cm^{-1} for **Pd-1** and **Pt-1** (Table S7†). This leads to negligible ISC rate constants (3.66×10^5 and 1.87×10^5 s^{-1} for **Pd-1** and **Pt-1**), much smaller than the radiative rate constants (8.11×10^6 and 5.13×10^6 s^{-1} for **Pd-1** and **Pt-1**) and non-radiative rates (4.04×10^7 and 7.46×10^7 s^{-1} for **Pd-1** and **Pt-1**). These results suggest that the small SOC, large ΔE_{ST} and the ligand-centered FMOs (Fig. S85†) are important factors for the non-population of the triplet state in Pd^{II} or Pt^{II} complexes.

To understand the $S_1 \rightarrow S_0$ process, we analyzed the Huang–Rhys factors as well as the displacement vectors of the vibrational modes with the largest Huang–Rhys factors (Fig. 5b, c and S88 details in the ESI†).[17] The most important non-radiative channels for **Pd-1** and **Pt-1** can be assigned to the torsional motion of the pentafluorophenyl group (with frequencies of 16.28 and 14.45 cm^{-1} in Fig. 5b and c). **Pt-1** has an additional non-negligible non-radiative channel (Fig. 5c), which is the out-plane vibration of the tripyrrin plane with a frequency of 22.12 cm^{-1}. This could be correlated to the dark state assigned to the structural relaxation observed in fs-TA for **Pt-1** in Fig. 4. Moreover, this out-plane vibration of tripyrrin plane can also be associated with the $1 \rightarrow 0$ band in the emission spectra according to the simulation of vibrationally resolved spectra (Fig. S89 and details in ESI†). This additional non-radiative channel leads to a larger non-radiative rate constant (7.46×10^7 s^{-1}, in Table S7†), compared with **Pd-1** (4.04×10^7 s^{-1}), and quenches the luminescence of **Pt-1** by a fast energy transfer (16.34 ps) in the luminescent S_1 state (Fig. 5d).

NIR bioimaging

As a proof-of-concept application, we herein introduced **Pd-1** and **Pd-3** into nanochannels of mesoporous silica nanoparticles, which endows fluorescent Pd^{II} complexes with excellent colloidal stability, low cytotoxicity, desirable blood circulation time and passive tumor-targeting ability by the enhanced permeability and retention (EPR) effects.[21] We prepared and characterized NIR fluorescent nanocapsules (**Pd-1-MSN-F127** and **Pd-3-MSN-F127**), by encapsulating **Pd-1** or **Pd-3** into mesoporous channels of silica nanoparticles following previous reports in the literature (Fig. 6a, S90 and S91†).[22] As expected, **Pd-1-MSN-F127** and **Pd-3-MSN-F127** display strong NIR emission centered at 717 and 771 nm in water solution,

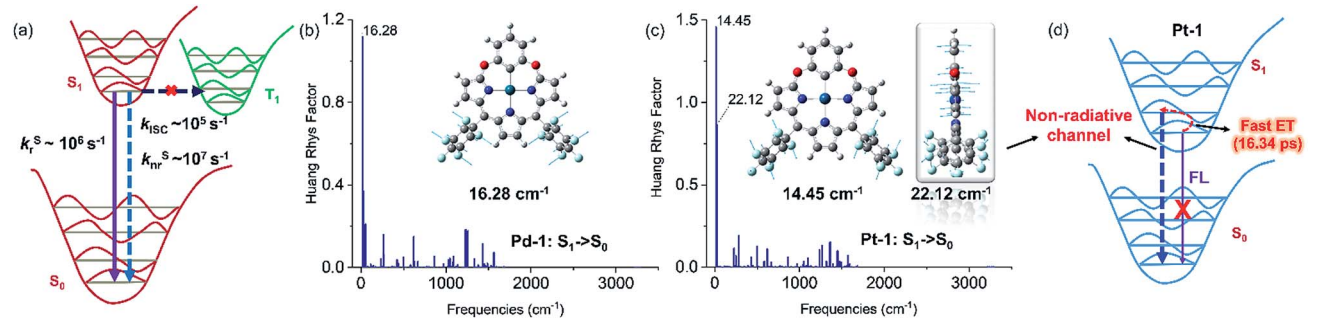

Fig. 5 (a) General illustration of the low-lying singlet and triplet excited states of **Pd-1** and **Pt-1**, and the calculated rate constants of different photophysical processes, in which the solid and dashed arrows represent radiative and non-radiative processes, respectively. Huang–Rhys factors for energy conversion between the S_1 and S_0 states of (b) **Pd-1** and (c) **Pt-1**, as well as the displacement vectors of important vibrational modes with the largest value of Huang–Rhys factor.[17] (d) Illustration of fluorescence quenching by the non-radiative channel in **Pt-1**.

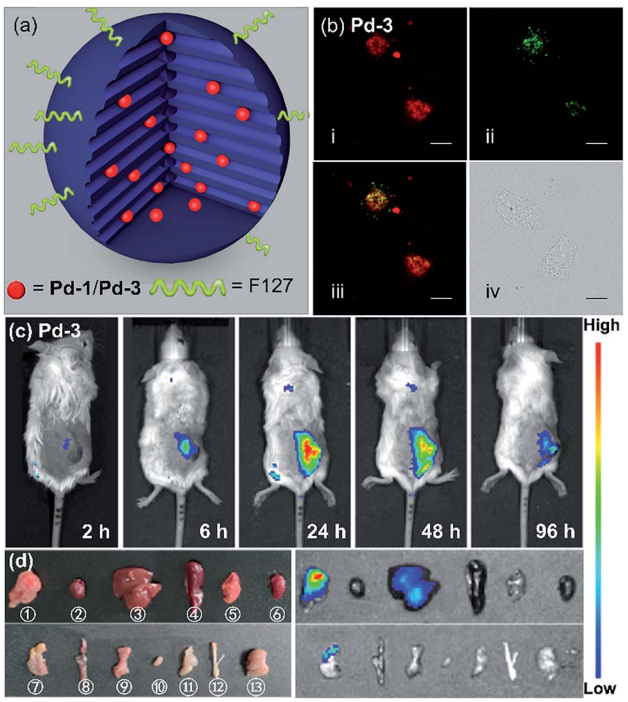

Fig. 6 (a) Sketch of the **Pd-1** and **Pd-3** in a single NIR-MSN-F127. (b) Confocal fluorescence image of (i) living HeLa cells with **Pd-3-MSN-F127** by the em > 776 nm channel under laser excitation at 700 nm; (ii) LysoTracker Green DND-26 excited at 488 nm, em = 525/50 channel; (iii) merged confocal fluorescence images of (i) and (ii); and (iv) differential interference contrast (DIC) images. Images of **Pd-3-MSN-F127** (incubated for 12 h) are presented with fake color; scale bar presents 20 μm. (c) Fluorescence imaging of 4T1 tumor-bearing mice after intravenous injection of **Pd-3-MSN-F127** at different time points. (d) Photograph (left) and fluorescence imaging (right) of main organs of 4T1 tumor-bearing mice at 96 h p.i. of **Pd-3-MSN-F127**. ①–⑬ stand for tumor, heart, liver, spleen, lung, kidney, stomach, intestine, pancreas, bladder, muscle, bone, and brain, respectively (λ_{ex} = 710 nm, λ_{em} = 776 nm).

upon excitation at 600 or 700 nm (Fig. S92–S95†). After verifying the high cell viability (Fig. S96†), we performed living cell imaging by incubation of **Pd-1-MSN-F127** (~10 μM) and **Pd-3-MSN-F127** (~10 μM) in living HeLa cells. As shown in Fig. S97† and 6b, distinct NIR fluorescence (700–000 nm) precisely co-localized with commercial LysoTracker Green DND-26 Dye (the Pearson coefficients were 0.74 and 0.80 for **Pd-1** and **Pd-3** respectively, Fig. S98†), suggesting the capability of **Pd-1** and **Pd-3** as NIR bioprobes for living cell imaging.

To demonstrate the application in *in vivo* bioimaging, we chose 4T1 tumor-bearing mice as our model. Each mouse was intravenously injected *via* the tail vein with **Pd-1-MSN-F127** or **Pd-3-MSN-F127** (100 μL, ~10 μM) and subjected to fluorescence imaging with 710 nm excitation and 776 nm emission at different time points. The luminescence signal was weak in 6 h (Fig. 6c and S99a†). After 24 h, we observed strong *in vivo* fluorescence, mainly accumulated specifically at the tumor site, as shown in Fig. 6c and S99a.† The mouse was sacrificed and dissected after 96 h post injection. *Ex vivo* fluorescence imaging as shown in Fig. S99b† and 6d displayed strong NIR fluorescence signals in the tumor and low intensity in the liver and stomach, indicating that **Pd-1-MSN-F127** or **Pd-3-MSN-F127** accumulated specifically at the tumor and was probably excreted through enterohepatic circulation and the digestive system. The sharp contrast of the tumor *versus* the remaining organs and tissues could be attributed to the strong fluorescence of **Pd-1-MSN-F127** or **Pd-3-MSN-F127**, their good stability and effective accumulation in tumors. Although more details about the long-term fate and clearance pathways remain unclear at the present stage, **Pd-1-MSN-F127** or **Pd-3-MSN-F127** are promising NIR candidate probes for *in vivo* bioimaging applications such as tumor diagnosis and imaging-guided surgery.

To further construct stimuli-responsive probes, we used **Pd-2**, which has weak fluorescence due to PET, to prepare a pH sensitive NIR probe (**Pd-2-MSN-F12**) by encapsulation of **Pd-2** into mesoporous silica nanoparticles. **Pd-2-MSN-F127** localized in the lysosome with a Pearson coefficient of 0.74 (Fig. 7a and S100†). From pH 5 to 10, **Pd-2-MSN-F127** exhibits a remarkable fluorescence increase of 4 fold and shows good reversibility (Fig. 7b–d, S100 and S101†). This could be assigned to the protonation of NMe_2 which inhibits the PET process and turns on the NIR fluorescence (Fig. 7b). To study the pH-sensitivity in living cells, we monitor the endogenous pH changes using the

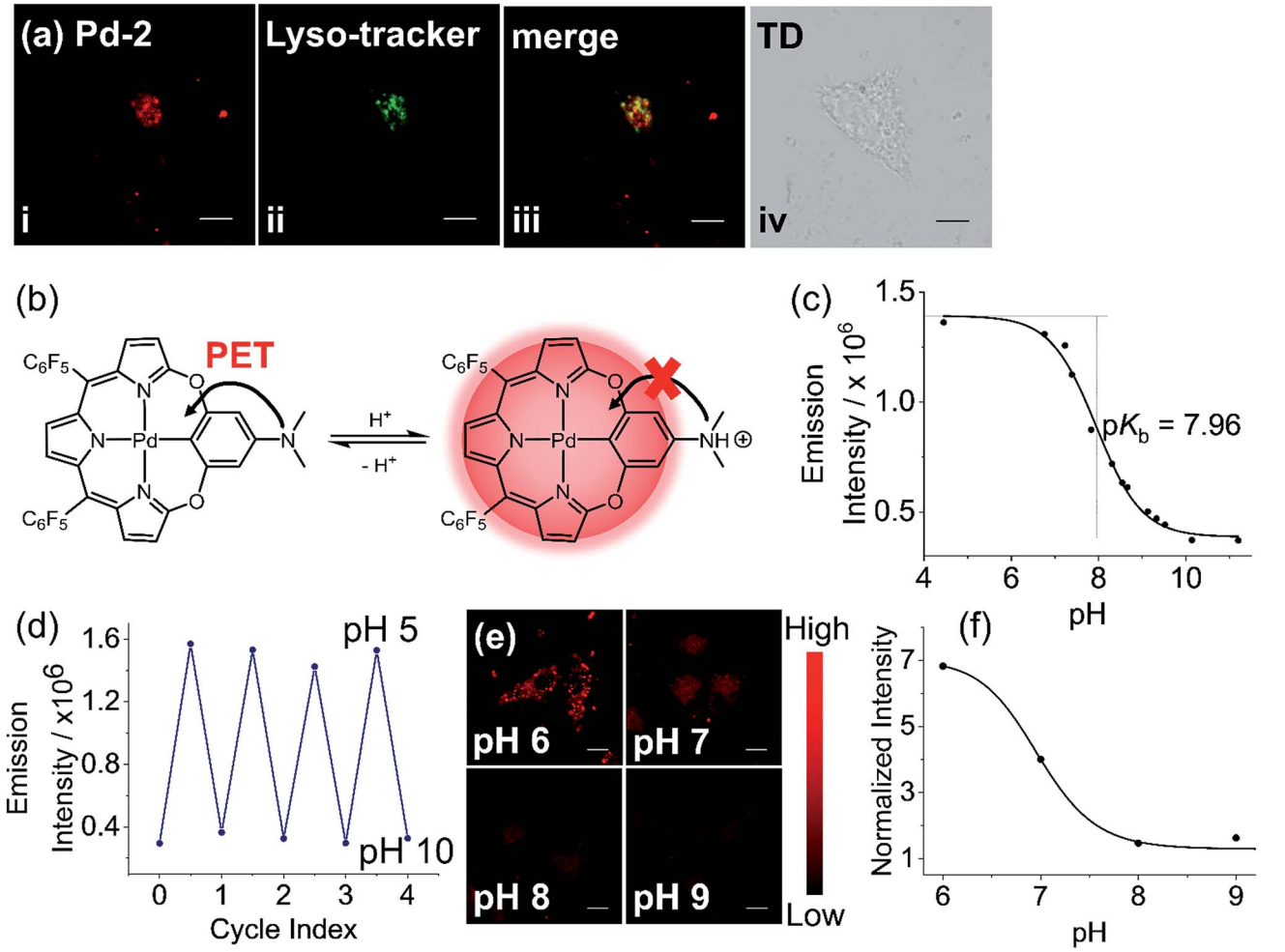

Fig. 7 (a) Confocal fluorescence image of (i) living HeLa cells with **Pd-2-MSN-F127** by em > 776 nm channel under laser excitation at 700 nm; (ii) LysoTracker Green DND-26 excited at 488 nm, em = 525/50 channel; (iii) merged confocal fluorescence images of (i) and (ii); and (iv) differential interference contrast (DIC) images. (b) Schematic view of pH sensitivity of **Pd-2** due to the switching on/off of photoinduced electron transfer (PET) by protonation. (c) Emission intensity of **Pd-2-MSN-F127** *versus* the pH values in the pH range 5–11. (d) Plot showing the reversible switching on/off of the emission of **Pd-2-MSN-F127** between pH 5 and 10. (e) Fluorescence imaging of **Pd-2-MSN-F127** at different pH values in pH range 6–9. (f) Dependence of normalized average intensity of fluorescence per cell on pH. Images of **Pd-2-MSN-F127** (incubated for 12 h) are presented with fake color; scale bar represents 20 μm.

antibiotic nigericin as an H^+/K^+ ionophore to induce H^+ efflux.[23] As shown in Fig. 7e, the intracellular NIR fluorescence intensity decreases as the pH is increased from 6 to 10 (Fig. 7f), similar to pH sensitive NIR emission in aqueous solution (Fig. 7c). These results demonstrate the capability of Pd complexes as a molecular platform to further design physiological stimuli-responsive NIR probes.

Conclusions

In summary, we designed and synthesized a series of new tetradentate macrocyclic benzitripyrrin C^N^N^N ligands (**1–5**) and the palladium(II) and platinum(II) complexes **Pd-1–3** and **Pt-3**. Coordination of Pd^{II} or Pt^{II} ion leads to a bathochromic shift of absorption and emission compared to the corresponding ligands, indicating that the metal chelating affects the ground- and excited-state structures. Importantly, chelating the Pd^{II} ion produces strong NIR fluorescence while no phosphorescence is observed, which is unusual for the previously reported Pd^{II} porphyrinoids or palladacycles. Femtosecond transient absorption spectra of **Pd-1** and **Pt-1** showed the intraligand (^{1}IL) charge transfer process and the nanosecond transient absorption spectra suggest no triplet states are populated. This could be attributed to a small SOC, arising from large singlet-triplet energy gaps and the ligand-centered FMOs, as suggested by the TDDFT calculation results. Additionally, the weak fluorescence of **Pt-1** can be ascribed to the non-radiative channel of the out-plane vibration of the tripyrrin plane, different from **Pd-1**. More importantly, we also demonstrated the strong NIR emission of Pd complexes (**Pd-1** and **Pd-3**) by encapsulation into mesoporous silica nanoparticles is advantageous compared to other phosphorescent metal complexes in *in vitro* or *in vivo* bioimaging because of much less oxygen interference. Finally, **Pd-2** was employed as a pH sensitive probe intracellularly,

demonstrating the potential of these Pd complexes as a molecular scaffold to design stimuli-responsive materials. Therefore, this work reveals the potential application of NIR fluorescent Pd complexes and promotes the development of Pd chemistry in biomedicine.

Ethical statement

All animal experiments were implemented in accordance with the Animal Management Rules of the Ministry of Health of the People's Republic of China (Document no. 55, 2001) and were approved and according to the guidelines from Laboratory Animal Ethics Committee of Peking University First Hospital (Peking University, China) (Approval ID: J201859).

Conflicts of interest

There are no conflicts to declare.

Acknowledgements

We thank the National Scientific Foundation of China (NSFC) (21571007, 21621061, 21778002, 21861162008) and the National Key Basic Research Support Foundation of China (NKBRSFC) (2015CB856301) for financial support. This work was supported by the High-performance Computing Platform of Peking University.

Notes and references

1 (*a*) G. Hong, A. L. Antaris and H. Dai, *Nat. Biomed. Eng.*, 2017, **1**, 0010; (*b*) R. R. Zhang, A. B. Schroeder, J. J. Grudzinski, E. L. Rosenthal, J. M. Warram, A. N. Pinchuk, K. W. Eliceiri, J. S. Kuo and J. P. Weichert, *Nat. Rev. Clin. Oncol.*, 2017, **14**, 347–364.

2 (*a*) W. Stummer, U. Pichlmeier, T. Meinel, O. D. Wiestler, F. Zanella, H. J. Reulen and A. L.-G. S. Group, *Lancet Oncol.*, 2006, **7**, 392–401; (*b*) V. Pansare, S. Hejazi, W. Faenza and R. K. Prud'homme, *Chem. Mater.*, 2012, **24**, 812–827; (*c*) G. Hong, S. Diao, A. L. Antaris and H. Dai, *Chem. Rev.*, 2015, **115**, 10816–10906; (*d*) S. Tsuboi, S. Yamada, Y. Nakane, T. Sakata, H. Yasuda and T. Jin, *ECS J. Solid State Sci. Technol.*, 2017, **7**, R3093–R3101; (*e*) G. Chen, Y. Zhang, C. Li, D. Huang, Q. Wang and Q. Wang, *Adv. Healthcare Mater.*, 2018, **7**, 1800497; (*f*) Y. Duan and B. Liu, *Adv. Mater.*, 2018, **30**, 1802394; (*g*) Q. Miao and K. Pu, *Adv. Mater.*, 2018, **30**, 1801778; (*h*) Y. Cai, Z. Wei, C. Song, C. Tang, W. Han and X. Dong, *Chem. Soc. Rev.*, 2019, **48**, 22–37; (*i*) F. Ding, Y. Fan, Y. Sun and F. Zhang, *Adv. Healthcare Mater.*, 2019, **8**, 1900260; (*j*) J. Li, H. Duan and K. Pu, *Adv. Mater.*, 2019, 1901607, DOI: 10.1002/adma.201901607; (*k*) S. Zhu, R. Tian, A. L. Antaris, X. Chen and H. Dai, *Adv. Mater.*, 2019, **31**, 1900321.

3 (*a*) S. He, J. Song, J. Qu and Z. Cheng, *Chem. Soc. Rev.*, 2018, **47**, 4258–4278; (*b*) F. Ding, Y. Zhan, X. Lu and Y. Sun, *Chem. Sci.*, 2018, **9**, 4370–4380.

4 (*a*) Y. Ning, S. Chen, H. Chen, J.-X. Wang, S. He, Y.-W. Liu, Z. Cheng and J.-L. Zhang, *Inorg. Chem. Front.*, 2019, **6**, 1962–1967; (*b*) Y. Ning, S. Cheng, J. X. Wang, Y. W. Liu, W. Feng, F. Li and J.-L. Zhang, *Chem. Sci.*, 2019, **10**, 4227–4235.

5 (*a*) E. Baggaley, J. A. Weinstein and J. A. G. Williams, *Coord. Chem. Rev.*, 2012, **256**, 1762–1785; (*b*) K. K. W. Lo, *Acc. Chem. Res.*, 2015, **48**, 2985–2995; (*c*) C. N. Ko, G. D. Li, C. H. Leung and D. L. Ma, *Coord. Chem. Rev.*, 2019, **381**, 79–103; (*d*) K. Q. Qiu, Y. Chen, T. W. Rees, L. N. Ji and H. Chao, *Coord. Chem. Rev.*, 2019, **378**, 66–86.

6 J. Dupont, C. S. Consorti and J. Spencer, *Chem. Rev.*, 2005, **105**, 2527–2571.

7 (*a*) P. K. Chow, C. Ma, W. P. To, G. S. Tong, S. L. Lai, S. C. Kui, W. M. Kwok and C.-M. Che, *Angew. Chem., Int. Ed.*, 2013, **52**, 11775–11779; (*b*) P. K. Chow, W. P. To, K. H. Low and C.-M. Che, *Chem.–Asian J.*, 2014, **9**, 534–545; (*c*) P. K. Chow, G. Cheng, G. S. M. Tong, C. Ma, W. M. Kwok, W. H. Ang, C. Y. Chung, C. Yang, F. Wang and C.-M. Che, *Chem. Sci.*, 2016, **7**, 6083–6098; (*d*) T. Fleetham, G. Li and J. Li, *Adv. Mater.*, 2017, **29**, 1601861; (*e*) Z. Q. Zhu, K. Klimes, S. Holloway and J. Li, *Adv. Mater.*, 2017, **29**, 1605002; (*f*) Q. Wan, W. P. To, C. Yang and C.-M. Che, *Angew. Chem., Int. Ed.*, 2018, **57**, 3089–3093; (*g*) G. Li, Z.-Q. Zhu, Q. Chen and J. Li, *Org. Electron.*, 2019, **69**, 135–152.

8 (*a*) H. Furuta, H. Maeda and A. Osuka, *Chem. Commun.*, 2002, 1795–1804, DOI: 10.1039/b200525p; (*b*) J. Harvey, *Coord. Chem. Rev.*, 2003, **247**, 1–19; (*c*) M. Stepien and L. Latos-Grazynski, *Acc. Chem. Res.*, 2005, **38**, 88–98; (*d*) T. D. Lash, *Acc. Chem. Res.*, 2016, **49**, 471–482; (*e*) T. D. Lash, *Chem. Rev.*, 2017, **117**, 2313–2446.

9 G. S. Tong, P. K. Chow and C.-M. Che, *Angew. Chem., Int. Ed.*, 2010, **49**, 9206–9209.

10 (*a*) J.-F. Wang, Y. Yao, Y. Ning, Y.-S. Meng, C.-L. Hou, J. Zhang and J.-L. Zhang, *Org. Chem. Front.*, 2018, **5**, 1877–1885; (*b*) C.-L. Hou, Y. Yao, D. Wang, J. Zhang and J.-L. Zhang, *Org. Chem. Front.*, 2019, **6**, 2266–2274.

11 (*a*) B. W. Pedersen, L. E. Sinks, T. Breitenbach, N. B. Schack, S. A. Vinogradov and P. R. Ogilby, *Photochem. Photobiol.*, 2011, **87**, 1077–1091; (*b*) W. P. To, Y. Liu, T. C. Lau and C.-M. Che, *Chem.–Eur. J.*, 2013, **19**, 5654–5664; (*c*) T. V. Esipova, H. J. Rivera-Jacquez, B. Weber, A. E. Masunov and S. A. Vinogradov, *J. Am. Chem. Soc.*, 2016, **138**, 15648–15662; (*d*) Z. Xun, Y. Zeng, J. Chen, T. Yu, X. Zhang, G. Yang and Y. Li, *Chem.–Eur. J.*, 2016, **22**, 8654–8662.

12 (*a*) M. L. Deda, M. Ghedini, I. Aiello, T. Pugliese, F. Barigelletti and G. Accorsi, *J. Organomet. Chem.*, 2005, **690**, 857–861; (*b*) V. Lakshmi, W.-Z. Lee and M. Ravikanth, *Dalton Trans.*, 2014, **43**, 16006–16014; (*c*) A. Kumar, S. Kumar, T. Chatterjee and M. Ravikanth, *ChemistrySelect*, 2016, **1**, 94–100; (*d*) S. Riese, M. Holzapfel, A. Schmiedel, I. Gert, D. Schmidt, F. Wurthner and C. Lambert, *Inorg. Chem.*, 2018, **57**, 12480–12488.

13 H. Weissman, E. Shirman, T. Ben-Moshe, R. Cohen, G. Leitus, L. J. Shimon and B. Rybtchinski, *Inorg. Chem.*, 2007, **46**, 4790–4792.

14 (*a*) A. P. de Silva, T. S. Moody and G. D. Wright, *Analyst*, 2009, **134**, 2385–2393; (*b*) E. M. Stennett, M. A. Ciuba and M. Levitus, *Chem. Soc. Rev.*, 2014, **43**, 1057–1075; (*c*) D. Escudero, *Acc. Chem. Res.*, 2016, **49**, 1816–1824.

15 M. Montalti, A. Credi, L. Prodi and M. T. Gandolfi, *Handbook of photochemistry*, CRC press, 2006.

16 (*a*) G. S. Tong, P. K. Chow, W. P. To, W. M. Kwok and C.-M. Che, *Chem.–Eur. J.*, 2014, **20**, 6433–6443; (*b*) K. T. Chana, G. S. M. Tong, W.-P. Toa, C. Yanga, L. Dub, D. L. Phillipsb and C.-M. Che, *Chem. Sci.*, 2016, **8**, 2352–2364; (*c*) Y. Bai, J. Rawson, S. A. Roget, J.-H. Olivier, J. Lin, P. Zhang, D. N. Beratan and M. J. Therien, *Chem. Sci.*, 2017, **8**, 5889–5901; (*d*) Y. Yao, H.-Y. Yin, Y. Ning, J. Wang, Y.-S. Meng, X. Huang, W. Zhang, L. Kang and J.-L. Zhang, *Inorg. Chem.*, 2019, **58**, 1806–1814.

17 Q. Peng, D. Fan, R. Duan, Y. Yi, Y. Niu, D. Wang and Z. Shuai, *J. Phys. Chem. C*, 2017, **121**, 13448–13456.

18 (*a*) T. Lu and F. Chen, *Acta Chim. Sin.*, 2011, **69**, 2393–2406; (*b*) T. Lu and F. Chen, *J. Comput. Chem.*, 2012, **33**, 580–592; (*c*) M. Xiao and T. Lu, *J. Adv. Phys. Chem.*, 2015, **4**, 111–124.

19 A. E. Reed and F. Weinhold, *J. Chem. Phys.*, 1985, **83**, 1736–1740.

20 (*a*) Z. G. Shuai, Q. Peng, Y. L. Niu and H. Geng, *MOMAP, a molecular materials property prediction package, revision 0.2.004*, Tsinghua University, Beijing, China, 2014, http://www.shuaigroup.net/; (*b*) Y. Niu, W. Li, P. Qian, G. Hua and Z. Shuai, *Mol. Phys.*, 2018, **116**, 1–13.

21 (*a*) M. P. Melancon, M. Zhou and C. Li, *Acc. Chem. Res.*, 2011, **44**, 947–956; (*b*) A. Z. Wang, R. Langer and O. C. Farokhzad, *Annu. Rev. Med.*, 2012, **63**, 185–198; (*c*) D. Tarn, C. E. Ashley, M. Xue, E. C. Carnes, J. I. Zink and C. J. Brinker, *Acc. Chem. Res.*, 2013, **46**, 792–801.

22 S. Mattiello, A. Monguzzi, J. Pedrini, M. Sassi, C. Villa, Y. Torrente, R. Marotta, F. Meinardi and L. Beverina, *Adv. Funct. Mater.*, 2016, **26**, 8447–8454.

23 (*a*) J. R. Casey, S. Grinstein and J. Orlowski, *Nat. Rev. Mol. Cell Biol.*, 2010, **11**, 50–61; (*b*) Y. Yue, F. Huo, S. Lee, C. Yin and J. Yoon, *Analyst*, 2016, **142**, 30–41.